https://doi.org/10.1016/j.apenergy.2021.116586

A simple but effective design to enhance the performance and durability of direct carbon solid oxide fuel cells

Wei Kong[1*], *Zhen Han*[1], *Siyu Lu*[1], *Meng Ni*[2*]

[1] School of Energy and Power, Jiangsu University of Science and Technology, 212003, Zhenjiang, Jiangsu, China;

[2] Building Energy Research Group, Department of Building and Real Estate, The Hong Kong Polytechnic University, Hung Hom, Kowloon, Hong Kong, China;

* Corresponding authors.

wkong@just.edu.cn (Wei Kong) ; meng.ni@ployu.edu.hk (Meng Ni)

Abstract. The development of high-performance and durable direct carbon solid oxide fuel cells requires that the rate of the Boudouard reaction is enhanced without significantly increasing the fuel cell temperature. Herein, a simple design is proposed to improve the performance of direct carbon solid oxide fuel cells by introducing a heat bar into the anode carbon compartment. This design is evaluated numerically using a 2D model. After model validation, parametric simulations are conducted to compare the performance of direct carbon solid oxide fuel cells with and without the heat bar. The heat bar improves the temperature uniformity of the fuel cell and enhances the local temperature in the carbon compartment. As a result, the Boudouard reaction rate is enhanced by 14% at a voltage of 0.6V, leading to a performance enhancement of 4.1%. The heat bar significantly reduces the difference between the maximum and minimum temperatures in the fuel cell by 40%, leading to improved durability. This design becomesmore effective when using a heat bar with a high thermal conductivity and at lower operating voltages. This study clearly demonstrates that this new design is a simple but effective method for enhancing the performance and durability of direct carbon solid oxide fuel cells.

Keywords: Direct carbon fuel cell; Solid oxide fuel cell; Boudouard reaction; Temperature; Carbon

1 Introduction

Recently, scholars have shown an increased interest in fuel cells [1]. Compared with low-temperature fuel cells, solid oxide fuel cells (SOFCs) have greater fuel flexibility. In addition to H_2, hydrocarbons can be used as fuel in SOFCs [2] because the high operating temperature allows internal reforming reactions and the water shift gas reactions to occur in the porous anode [3]. Furthermore, direct carbon SOFCs (DC-SOFCs), which can directly use solid carbon as a fuel with high efficiency and low pollution, have received widespread attention in recent years, as carbon is a key component of coal and renewable biomass [4]. The successful development of DC-SOFCs indicates that coal and renewable biomass can potentially be used in SOFCs for power generation.

In DC-SOFCs, the solid carbon particles are larger than the pore sizes of SOFC anodes. As the carbon particles cannot enter the porous anode, carbon is not electrochemically oxidized. Instead, carbon is gasified by CO_2 (reversible Boudouard reaction) to produce CO, which subsequently diffus into the DC-SOFC anode for electrochemical reaction. This “CO shuttle effect” was verified experimentally by Xie et al. [5]. Owing to this mechanism, the performance of DC-SOFCs is highly dependent on the Boudouard reaction rate, which has been widely studied. Wang et al. successfully fabricated a tubular DC-SOFC that, produced a maximum power density of 104 mW cm^{-2} at 850 °C [6]. However, the experimental data showed that insufficient CO as fuel is a critical factor that limits the cell performance owing to a low Boudouard reaction rate.

To enhance the Boudouard reaction rate, many researchers have focused on developing effective catalysts[7]. Compared with carbon without a catalyst, Fe-loaded[8], Ca-loaded[9], Ba-loaded[10], K-loaded[11], and steel-slag-loaded[12] carbon can significantly enhance the Boudouard reaction rate. Xu et al. investigated the effect of catalysts on DC-SOFC performance and reported that the maximum power density could be increased by 53.3% by using a suitable catalyst to enhance the Boudouard reaction [13]. Shao et al. reported that the Boudouard reaction rate is closely related to the solid carbon surface area [14]. The Boudouard reaction rate was 4.81 mmol (min g)$^{-1}$ at 850 °C for carbon with a surface area of 1214.2 m^2 g^{-1}, whereas it decreased to 0.21 mmol (min g)$^{-1}$ with a surface area of 227.4 m^2 g^{-1}.

Furthermore, as the Boudouard reaction is endothermic, a high temperature is needed to achieve a high reaction rate. For example, the Boudouard reaction rate was increased from 0.024 to 0.21 mmol (min g)$^{-1}$ by increasing the temperature from 750 to 850 °C. Xu et al. developed a 2D tubular DC-SOFCisothermal numerical model and demonstrated that the cell performance was enhanced at higher operating temperatures owing to an increase in the Boudouard reaction rate [15]. Xu et al. [16] also investigated the effect of operating and structural parameters on the temperature distribution in DC-SOFCs and observed that the temperature distribution is highly non-uniform. The influence of CO-CO_2 counter diffusion on the Boudouard reaction was experimentally studied by Zhou et al. [17],who found that a smaller distance between the anode and carbon increased the output power density. These studies clearly demonstrate that the performance of DC-SOFCs strongly depends on the operating temperature. The endothermic nature of the Boudouard reaction could cause the temperature of the carbon compartment to be lower than the temperature of the DC-SOFC, thus hingering performance. Although increasing the operating temperature of the DC-SOFC would increase the temperature of the carbon compartment and thus improve performance, a high temperature can result in poor long-term stability for DC-SOFCs. Thus, enhancingt the Boudouard reaction rate without significantly increasing the DC-SOFC temperature is critical for developing high-performance and durable DC-SOFCs.

Although there are numerous experimental studies on developing suitable catalysts for the Boudouard reaction, few studies have focused on engineering designs to improve the Boudouard reaction. In this work, a simple design is proposed to insert a heat bar into the anode carbon compartment of a DC-SOFC, as shown in Fig. 1(a). The heat bar is expected to increase the temperature of the carbon compartment, without increasing the temperature of the DC-SOFC. To evaluate the effectiveness of this new design, two 2D multi-physics coupling numerical models were developed for tubular DC-SOFCs without and with a heat bar, and the heat bar thermal conductivity, heat bar radius, and carbon compartment porosity were considered. The results indicated that the heat bar aids in maintaining a relatively high local temperature in the carbon compartment, which is beneficial to the Boudouard reaction and thus enhances DC-SOFC performance. In addition, the heat bar improved the temperature uniformity of the DC-SOFC, leading to better durability. The present study clearly demonstrated that the proposed design is a simple but effective method for enhancing the performance and durability of DC-SOFCs.

2 Model

2.1 Model geometry

The conventional tubular DC-SOFC consists of a cathode, an anode, an electrolyte and a carbon chamber. To increase the local temperature of the carbon chamber, a novel tubular DC-SOFC with a heat bar in the anode carbon compartment is proposed, as shown in Fig. 1(a). Based on the symmetry of this design, two 2D axial symmetry models were established for tubular DC-SOFCs with and without a heat bar. Fig. 1(b) illustrates the model geometry and size, which is consistent with the configuration in Ref. [8].

2.2 Governing equations

The model used in this work considered the electrochemical reaction, charge transport, momentum transport, mass transport, and heat transport. In addition, the Boudouard reaction was also considered. The adopted model parameters are listed in Table 1-3.

2.2.1 Electrochemical reaction model

The electrochemical reaction rate is determined by the Butler-Volmer equation. For anode and cathode, the Butler-Volmer equation can be expressed as[18]:

$$i_{trans}^{an} = i_{ref}^{an} \exp\left(-\frac{E_{CO}}{R}\left(\frac{1}{T} - \frac{1}{T_{ref}} \right) \right)\left(\frac{p_{CO}^{TPB}\, p_{CO_2}^{TPB}}{p_{CO}^{0}\, p_{CO_2}^{0}} \right) \times \left[\exp\left(\frac{2\alpha_f^{an} F}{RT}\eta_{act}^{an} \right) - \exp\left(-\frac{2\beta_r^{an} F}{RT}\eta_{act}^{an} \right) \right] \quad (1)$$

$$i_{trans}^{ca} = i_{ref}^{ca} \exp\left(-\frac{E_{O_2}}{R}\left(\frac{1}{T} - \frac{1}{T_{ref}} \right) \right)\left(\frac{p_{O_2}^{TPB}}{p_{O_2}^{0}} \right)^{0.25} \times \left[\exp\left(\frac{2\alpha_f^{ca} F}{RT}\eta_{act}^{ca} \right) - \exp\left(-\frac{2\beta_r^{ca} F}{RT}\eta_{act}^{ca} \right) \right] \quad (2)$$

Here i_{trans}^{an} (i_{trans}^{ca}) is the conversion current of the anode (cathode); T_{ref} is the reference temperature; E_{CO} (E_{O_2}) is the activation energy of CO (O_2); i_{ref}^{an} (i_{ref}^{ca}) is the reference exchange current density of the anode (cathode); α_f and β_r are reaction symmetry factors; P_{CO}^{TPB}, $P_{CO_2}^{TPB}$ and $P_{O_2}^{TPB}$ are the species partial pressures at the three-phase boundary (TPB) reaction sites, where ions, electrons and gaseous species are in contact with each other; P_{CO}^{0}, $P_{CO_2}^{0}$ and $P_{O_2}^{0}$ are the initial species partial pressures; T is the temperature; R is the gas constant; F is the Faraday constant; and η_{act}^{an} (η_{act}^{ca}) is the activation polarization of the anode (cathode), which is defined as:

$$\eta_{act}^{an} = \varphi_{el} - \varphi_{io} - Eq_{an} \quad (3)$$

$$\eta_{act}^{ca} = \varphi_{el} - \varphi_{io} - Eq_{ca} \quad (4)$$

Here φ_{el} and φ_{io} are the local electronic and ionic potentials, respectively, and Eq_{an} (Eq_{ca}) is the equilibrium potential of the anode (cathode). The expressions for Eq_{an} and Eq_{ca} can be found in Refs. [13].

2.2.2 Charge transport

The ion and electron current densities are determined using the following charge conservation equations:

$$\nabla \cdot i_{io} = \nabla \cdot \left(-\sigma_{io}^{eff} \nabla \varphi_{io} \right) = \begin{cases} \lambda_{TPB} i_{trans}^{ca} & Cathode \\ \\ \lambda_{TPB} i_{trans}^{an} & Anode \end{cases} \tag{5}$$

$$\nabla \cdot i_{el} = \nabla \cdot \left(-\sigma_{el}^{eff} \nabla \varphi_{el} \right) == \begin{cases} -\lambda_{TPB} i_{trans}^{ca} & Cathode \\ \\ -\lambda_{TPB} i_{trans}^{an} & Anode \end{cases} \tag{6}$$

where i_{io} (i_{el}) is the ion (electron) current density, λ_{TPB} is the length of the TPB, and σ_{io}^{eff} (σ_{el}^{eff})is the effective ion (electron) conductivity. The expressions for σ_{io}^{eff} and σ_{el}^{eff} are given in Ref. [15].

2.2.3 Momentum and mass transport

The Navier–Stokes equation is employed to describe momentum transport in the gas channel, as follows:

$$(\rho u \nabla) u = -\nabla p + \nabla[\mu(\nabla u + (\nabla u)^T) - \frac{2}{3}\mu \nabla u] \tag{7}$$

As shown in Eq. (8), for a porous carbon chamber and electrodes, the modified Navier–Stokes equation in combination with Darcy's term is used to describe momentum transport.

$$(\rho u \nabla) u = -\nabla p + \nabla[\mu(\nabla u + (\nabla u)^T) - \frac{2}{3}\mu \nabla u] - \frac{\varepsilon \mu u}{B_0} \tag{8}$$

where ρ is the gas density, u is the velocity vector, ε is the porosity, B_0 is the permeability coefficient,and μ is the viscosity coefficient, The expression foro μ found in Ref. [15] was adopted in this study.

Gas transport in the channel is described by Fick's law, which can be written as [18]:

$$N_i = -D_{ij} \nabla c_i + c_i u \tag{9}$$

The molar flow of gas in electrodes is determined by considering Knudsen diffusion, molecular diffusion, and viscous flow, as follows:

$$N_i = -\frac{\varepsilon}{\tau}\frac{D_{ij}D_{iKn}}{D_{ij} + x_i D_{jKn} + x_j D_{iKn}}\nabla c_i + c_i u \tag{10}$$

However, in the present system, Knudsen diffusion could be ignored owing to the large pore size in the carbon chamber. Thus, the molar flow of gas in the carbon chamber is expressed as:

$$N_i = -\frac{\varepsilon}{\tau}D_{ij}\nabla c_i + c_i u \tag{11}$$

where N_i is the molar flow rate of gas *i*; τ is the tortuosity; x_i and c_i are the mole fraction and molar concentration of gas *i* respectively; and D_{ij} and D_{iKn} are the binary diffusion coefficient and Knudsen diffusion coefficient, respectively. The widely used formulae for D_{ij} and D_{iKn} were adopted, as detailed in Ref. [19].

2.2.4 Heat transfer

The energy conservation equation was adopted to simulate heat transfer in the DC-SOFC, as follows:

$$\nabla(-K_{eff}\nabla T + \rho C_P u T) = \begin{cases} Q_{ohm} + Q_{act} + Q_s & Electrode \\ Q_{ohm} & Electrolyte \\ Q_{rb} & Carbon\ chamber \end{cases} \tag{12}$$

where C_p is the specific heat capacity and K_{eff} is the effective thermal conductivity. The ohmic heat source Q_{ohm}, active heat source Q_{act}, and entropy heat source Q_{entr} can be calculated as:

$$Q_{ohm} = \frac{i_{el}^2}{\sigma_{el}^{eff}} + \frac{i_{io}^2}{\sigma_{io}^{eff}} \tag{13}$$

$$Q_{act} = \lambda_{TPB} i_{trans} \eta_{act} \tag{14}$$

$$Q_{entr} = \lambda_{TPB} i_{trans} (-\frac{T\Delta S}{2F}) \tag{15}$$

where S is the entropy and the heat absorption of the carbon chamber (Q_{rb}) is equal to the enthalpy change of the Boudouard reaction [20].

2.2.5 Chemical model

Unlike conventional SOFCs, the fuel used in DC-SOFCs is solid carbon. However, the species that participates in the electrochemical reaction is actually CO; thus, the Boudouard reaction (Eq. (16)) is significant for DC-SOFCs [21].

$$C + CO_2 \leftrightarrow 2CO \tag{16}$$

The rate of the Boudouard reaction (R_{rb}) can be calculated using Eq. (17) [16]:

$$R_{rb} = k_{rb} c_{co_2} \exp(-E_{rb} / RT) \tag{17}$$

where k_{rb} is the equilibrium constant, E_{rb} is the activation energy of the Boudouard reaction, and c_{co_2} is the local concentration of CO_2.

2.2.6 Boundary conditions

Owing to the complex coupling of many of the equations, reasonable boundary conditions must be set. The detailed boundary conditions are summarized in Table 4.

3 Results and discussion

3.1 Model validation

The developed models were established using the commercial software Comsol Multiphysics®. The validation of model was conducted for DC-SOFC with different fuels. The models with wheat straw char and Ca-loaded wheat straw char as the fuel were developed based on the Ref.[22]. The detailed setting of models can be found in supporting information. Another model fueled with Fe-loaded carbon was established according to the experimental condition in the Ref. [8]. The detailed described of model is given in supporting information. The model results were compared with the experimental data, as shown in Fig. 2. The good agreement between the model results and the experimental data confirms the accuracy of the present model. In the following sections, the parameters in Table 1 and 3 are used unless otherwise specified.

3.2 Comparison of tubular DC-SOFCs without and with heat bar

The temperature distribution in a DC-SOFC is highly non-uniform. The low-temperature region in the anode carbon compartment hinders the Boudouard reaction. Thus, a DC-SOFC with a heat bar in the anode carbon compartment was proposed. A comparison of the DC-SOFCs without and with a heat bar showed that the minimum temperature of 861.4 °C was increased to 922.8 °Cby the introduction of the heat bar. The increased local temperature in the carbon compartment enhanced the Boudouard reaction, which in turn improved the performance of the DC-SOFC by 4.1%. The significant difference between the cases without and with the heat bar can be explained by the temperature and CO distributions.

Fig. 3(a) depicts the temperature distributions in the carbon chambers without and with the heat bar. As expected, the temperature increases from the bottom to the top of the cell along the air flow direction, which is consistent with the numerical results reported by Xu et al. [16]. The minimum temperature with the heat bar is higher than that without the heat bar because the heat generated by the electrochemical reaction can be transferred from the top to the bottom of the cell through the heat bar. The relatively higher minimum temperature with the heat bar is favorable for the Boudouard reaction. As a result, the minimum CO mass fraction is 0.91, which is much higher than the without the heat bar (0.85), as shown in Fig. 3(b). In addition, the CO mass fraction is relatively smaller near the anode surface becauseCO is consumed in the electrochemical reaction.

Fig. 4(a) shows the temperature distribution at the anode surface. The maximum temperature is 1090 °C without the heat bar but 1060.5 °Cwith the heat bar. However, the temperature on most of the anode surface is higher when the heat bar is present. Therefore, the inserted heat bar promotes heat transfer in the carbon chamber, reduces the maximum temperature, and enhances the minimum temperature (local temperature in the carbon compartment), resulting in a more uniform temperature field. Moreover, the maximum temperature difference with heat bar is approximately 40% lower than that without the heat bar. Owing to the relatively uniform temperature field ontained with the heat bar, the maximum difference in the CO mass fraction is smaller than that in the case without the heat bar, as depicted in Fig. 4(b). Thus, relatively uniform temperature and species fields are achieved with the heat bar, which are beneficial for the stable operation of DC-SOFCs.

As shown in Fig. 1, the cathode has a length of 90 mm (Z = 0 90 mm) and is shorter than the other parts of the tubular DC-SOFC. Therefore, the electrochemical reaction does not occur in the regions of $Z < 0$ mm or $Z > 90$ mm. However, the Boudouard reaction still occurs in these regions through the absorption of large amounts of heat. For this reason, the temperature decreases at $Z > 80$ mm and the CO mass fraction increases near Z = 0 or 90 mm.

The average volumetric Boudouard reaction rate R_{rb} of the carbon chamber is shown in Fig. 5. R_{rb} increases sharply as the operating voltage V_{op} decreases. A lower operating voltage result in a higher average temperature owing to the increase heat produced by the electrochemical reaction, which accelerates the Boudouard reaction. In addition, the R_{rb} values with the heat bar at V_{op} = 0.6, 0.7, and 0.8 V were 14%, 12.9% and 11.1% respectively, higher than the corresponding values without the heat bar. These result suggest that the inserted heat bar can enhance the overall Boudouard reaction rate over a wide range of operating voltages.

To illustrate the advantage of using the heat bar, the growth rate γ_{i} was defined as shown in Eq. (18).

$$\gamma_{\mathrm{i}} = \frac{I_{with} - I_{without}}{I_{without}} \tag{18}$$

where I_{with} ($I_{without}$) is the output current density with (without) the heat bar.

3.3 Effect of heat bar thermal conductivity

Heat bars can be fabricated using many different materials such as Cu, Fe, Ni, and Co, and the thermal conductivity of the heat bar K is strongly dependent on the chosen material. Thus, it is necessary to examine the effect of heat bar thermal conductivity on the growth rate γ_{i}. As shown in Fig. 6, for a fixed V_{op}, γ_{i} increases with the increase in K. For example, at an operating voltage of 0.6 V, the γ_{i} value for $K = 3500\ \mathrm{Wm^{-1}K^{-1}}$ is almost 2.5 times larger than that for $K = 35\ \mathrm{W\ m^{-1}\ K^{-1}}$. Clearly, a smaller heat resistance allows more heat flux to be transferred from the top to the bottom of the cell via the heat bar. Therefore, a more uniform temperature field is achieved by using a heat bar with a higher thermal conductivity, as shown in Fig. 7. The maximum temperature difference is 210.98 °C for $K = 35\ \mathrm{W\ m^{-1}\ K^{-1}}$ but 94.15 °C for $K = 3500\ \mathrm{W\ m^{-1}\ K^{-1}}$. According to this analysis, the use of high thermal conductivity materials for the heat bar is recommended to optimize the performance of DC-SOFCs.

3.4 Effect of heat bar radius

The radius of the heat bar R_{hb} also plays an important role in improving the cell performance. Similar to the trend observed for the heat bar thermal conductivity K, at all operating voltages, the γ_{i} value increases as R_{hb} increases(Fig. 8). A larger heat bar is advantageous for heat transfer and thus increase the local temperature in the carbon chamber. However, for a tubular DC-SOFC with a fixed inner diameter, the heat absorbed by the Boudouard reaction decreases as the radius of the heat bar increases owing to the reduction in the volume of carbon. As a result, the average temperature increases, especially in the carbon compartment, which promotes the Boudouard reaction. For instance, the average volumetric Boudouard reaction rate at 0.7 V is enhanced by 22.4% when R_{hb} is increased from 1 to 3 mm.

3.5 Effect of carbon chamber porosity

Fig. 9 illustrates the effect of the carbon chamber porosity on γ_{i}. For different carbon chamber porosities, the γ_i values are similar. Thus, the carbon chamber porosity has a very limited impact on γ_i. As carbon is consumed, the carbon chamber porosity increases, which enhances fuel transport in the carbon chamber and promotes the Boudouard reaction. However, the increase in porosity also reduces the amount of carbon, which limits the Boudouard reaction. Moreover, the γ_i value increases as the operating voltage decreases, which suggests that the effect of the heat bar is more pronounced at lower operating voltages.

4 Conclusions

In this work, the insertion of a heat bar in the anode carbon compartment of a direct carbon solid oxide fuel cell (DC-SOFC) was proposed. A comparison of DC-SOFCs without and with a heat bar using a simulation method revealed the significant effects of the heat bar. The main conclusions are as follows:

(1) The minimum temperature and CO mass fraction increase because heat is easily transferred from the top to the bottom of the cell through the heat bar.

(2) More uniform temperature and CO distribution are obtained with the heat bar, which are beneficial for the stable operation of DC-SOFCs.

(3) At 0.6 V, the inserted heat bar significantly enhances the overall Boudouard reaction rate by 14% and the cell performance by 4.1%.

(4) The introduction of a heat bar into DC-SOFCs provides obvious advantages, especially at higher heat bar thermal conductivities or lower operating voltages.

Acknowledgments We gratefully acknowledge financial support from the Zhenjiang Key Laboratory of Marine Power Equipment Performance (SS2018006), the National Science Foundation of China (21406095), and the Natural Science Foundation of Jiangsu Province, China (BK20180982). M. Ni is thankful for funding from The Hong Kong Polytechnic University (G-YW2D) and grants (Project Number: PolyU 152214/17E and PolyU

152064/18E) from the Research Grant Council, University Grants Committee, Hong Kong SAR.

References

[1] Chen D, Xu Y, Hu B, Yan C, Lu L. Investigation of proper external air flow path for tubular fuel cell stacks with an anode support feature. Energy Conversion and Management. 2018;171:807-14.
[2] Xie H, Zhai S, Chen B, Liu T, Zhang Y, Ni M, et al. Coal pretreatment and Ag-infiltrated anode for high-performance hybrid direct coal fuel cell. Appl Energy. 2020;260:114197.
[3] van Biert L, Visser K, Aravind PV. A comparison of steam reforming concepts in solid oxide fuel cell systems. Appl Energy. 2020;264:16.
[4] Wu H, Xiao J, Zeng X, Li X, Yang J, Zou Y, et al. A high performance direct carbon solid oxide fuel cell – A green pathway for brown coal utilization. Appl Energy. 2019;248:679-87.
[5] Xie Y, Tang Y, Liu J. A verification of the reaction mechanism of direct carbon solid oxide fuel cells. Journal of Solid State Electrochemistry. 2012;17:121-7.
[6] Liu R, Zhao C, Li J, Zeng F, Wang S, Wen T, et al. A novel direct carbon fuel cell by approach of tubular solid oxide fuel cells. Journal of Power Sources. 2010;195:480-2.
[7] Tang Y, Liu J. Effect of anode and Boudouard reaction catalysts on the performance of direct carbon solid oxide fuel cells. International Journal of Hydrogen Energy. 2010;35:11188-93.
[8] Cai W, Liu J, Xie Y, Xiao J, Liu M. An investigation on the kinetics of direct carbon solid oxide fuel cells. Journal of Solid State Electrochemistry. 2016;20:2207-16.
[9] Cai W, Liu J, Yu F, Zhou Q, Zhang Y, Wang X, et al. A high performance direct carbon solid oxide fuel cell fueled by Ca-loaded activated carbon. International Journal of Hydrogen Energy. 2017;42:21167-76.
[10] Tang H, Yu F, Wang Y, Xie Y, Meng X, Sun H, et al. Enhancing the Power Output of Direct Carbon Solid Oxide Fuel Cell Using Ba ‐ Loaded Activated Carbon Fuel. Energy Technology. 2019;7:1800885.
[11] Yu X, Shi Y, Wang H, Cai N, Li C, Ghoniem AF. Using potassium catalytic gasification to improve the performance of solid oxide direct carbon fuel cells: Experimental characterization and elementary reaction modeling. Journal of Power Sources. 2014;252:130-7.
[12] Jiao Y, Wang C, Zhang L, An W, Zhou N, Yang G, et al. A steel slag–derived Boudouard reaction catalyst for improved performance of direct carbon solid oxide fuel cells. International Journal of Energy Research. 2019.

[13] Xu H, Chen B, Zhang H, Tan P, Yang G, Irvine JTS, et al. Experimental and modeling study of high performance direct carbon solid oxide fuel cell with in situ catalytic steam-carbon gasification reaction. Journal of Power Sources. 2018;382:135-43.
[14] Wu Y, Su C, Zhang C, Ran R, Shao Z. A new carbon fuel cell with high power output by integrating with in situ catalytic reverse Boudouard reaction. Electrochemistry Communications. 2009;11:1265-8.
[15] Xu H, Chen B, Liu J, Ni M. Modeling of direct carbon solid oxide fuel cell for CO and electricity cogeneration. Appl Energy. 2016;178:353-62.
[16] Xu H, Chen B, Zhang H, Kong W, Liang B, Ni M. The thermal effect in direct carbon solid oxide fuel cells. Applied Thermal Engineering. 2017;118:652-62.
[17] Zhou M, Wang X, Zhang Y, Qiu Q, Liu M, Liu J. Effect of counter diffusion of CO and CO2 between carbon and anode on the performance of direct carbon solid oxide fuel cells. Solid State Ionics. 2019;343:115127.
[18] Kong W, Han Z, Lu S, Gao X, Wang X. A novel interconnector design of SOFC. International Journal of Hydrogen Energy. 2019.
[19] Su S, Zhang Q, Gao X, Periasamy V, Kong W. Effects of changes in solid oxide fuel cell electrode thickness on ohmic and concentration polarizations. International Journal of Hydrogen Energy. 2016;41:16181-90.
[20] Xu H, Chen B, Tan P, Zhang H, Yuan J, Liu J, et al. Performance improvement of a direct carbon solid oxide fuel cell system by combining with a Stirling cycle. Energy. 2017;140:979-87.
[21] Liu J, Zhou M, Zhang Y, Liu P, Liu Z, Xie Y, et al. Electrochemical Oxidation of Carbon at High Temperature: Principles and Applications. Energy & Fuels. 2017;32:4107-17.
[22] Cai W, Liu J, Liu P, Liu Z, Xu H, Chen B, et al. A direct carbon solid oxide fuel cell fueled with char from wheat straw. International Journal of Energy Research. 2018.
[23] Huang H, Han Z, Lu S, Kong W, Wu J, Wang X. The analysis of structure parameters of MOLB type solid oxide fuel cell. International Journal of Hydrogen Energy. 2019.
[24] Eguchi K, Setoguchi T, Inoue T, H. A. Electrical-properties of ceria-based oxides and their application to solid oxide fuel-cells. Solid State Ionics. 1992;52:165-72.
[25] Kong W, Gao X, Liu S, Su S, Chen D. Optimization of the Interconnect Ribs for a Cathode-Supported Solid Oxide Fuel Cell. Energies. 2014;7:295-313.

List of Tables

Table 1 Model basic parameters

Parameter	Equations or values	Unit
i_{ref}^{an}, i_{ref}^{ca}	1.5 × 10^{-3}, 0.5 × 10^{-4}	A m^{-1}
α_f^{an}, β_r^{an}	0.5, 0.6	
α_f^{ca}, β_r^{ca}	0.5, 0.6	
E_{CO}, E_{O_2} [23]	120 × 10^3, 130 × 10^3	J mol^{-1}
P_{CO}^0, $P_{CO_2}^0$, $P_{O_2}^0$	95222, 6078, 21273	Pa
T_{ref} [23]	1073.15	K
ε	0.5 (carbon chamber)	
τ	3	
B_0 [18]	1.76 × 10^{-10}	m^2
E_{rb} [15]	248	kJ mol^{-1}
Output voltage	0.6	V
Intrinsic conductivity (σ)		
Ag[15]	$\dfrac{1.59e^8}{(0.0038T-0.1134)}$	S m^{-1}
GDC[24]	$\dfrac{100}{T}\times 10^{\left(6.66071-\frac{5322.92}{T}\right)}$	S m^{-1}
YSZ[25]	$6.25\times 10^4 \exp(\dfrac{-10300}{T})$	S m^{-1}
Thermal conductivity (K_{eff})[16]		
Electrode	13.54	W m^{-1} K^{-1}
Electrolyte	2.7	W m^{-1} K^{-1}
Carbon	1.59	W m^{-1} K^{-1}
Heat bar	350	W m^{-1} K^{-1}
Specific heat capacity (C_p)[16]		
Electrode	390	J kg^{-1} K^{-1}
Electrolyte	300	J kg^{-1} K^{-1}
Carbon	887.5	J kg^{-1} K^{-1}
Heat bar	451	J kg^{-1} K^{-1}
Density (ρ)[16]		
Electrode	6870	kg m^{-3}
Electrolyte	2000	kg m^{-3}
Carbon	1700	kg m^{-3}
Heat bar	8900	kg m^{-3}

Table 2 Parameters for model with (Ca-loaded) wheat straw char

Parameter	Equations or values	Unit
The equilibrium constant of Boudouard reaction k_{rb}		

wheat straw char	$1.92\times10^{13}\dfrac{T-973}{150}$	s^{-1}
Ca-loaded wheat straw char	$4.2\times10^{13}\dfrac{T-973}{150}$	s^{-1}
Temperature	800	℃
Volume fraction in electrode		
GDC	0.21	
Ag	0.79	
λ_{TPB}	2.71×10^{12}	$m^2\ m^{-3}$
Porosity (ε)		
Anode	0.46	
Cathode	0.46	

Table 3 Parameters for model with Fe-loaded carbon

Parameter	Equations or values	Unit
The equilibrium constant of Boudouard reaction k_{rb}		
Fe-loaded carbon	$6\times10^{13}\dfrac{T-973}{150}$	s^{-1}
Temperature	850	℃
Volume fraction in electrode		
GDC	0.21	
Ag	0.79	
λ_{TPB}	2.71×10^{12}	$m^2\ m^{-3}$
Porosity (ε)		
Anode	0.46	
Cathode	0.46	

Table 4 Boundary conditions

Equation	Channel inlet	Electrode/electrolyte interface		Channel outlet	Other
	Species concentration	Species molar flow			
Fuel transport	-	CO: $-i_{\mathrm{trans}}^{\mathrm{an}}/2F$	CO2: $i_{\mathrm{trans}}^{\mathrm{an}}/2F$	$\vec{n}\bullet(-D_i\nabla C_i)=0$	Insulation
Air transport	$c_{\mathrm{O_2}}^{0}$ $c_{\mathrm{N_2}}^{0}$	O2: $i_{\mathrm{trans}}^{\mathrm{ca}}/4F$	N2: 0	$\vec{n}\bullet(-D_i\nabla C_i)=0$	Insulation
Momentum transport	Channel inlet		Channel outlet		Other
	Inlet velocity		Pressure outlet		
	0 (fuel); 5 m/s (air)		1 atm (fuel); 1 atm (air)		No slip
Heat transfer	Channel inlet		Channel outlet		Other
	Temperature				
	850 °C		$\vec{n}\bullet(-K_{eff}\nabla T)=0$		Insulation
	Anode outside surface	Cathode outside surface	Anode/electrolyte interface	Cathode/electrolyte interface	Other
Electronic transport	0	V_{op}	$-\lambda_{TPB}^{A}i_{trans}^{an}$	$-\lambda_{TPB}^{A}i_{trans}^{ca}$	Insulation
Ionic transport	-	-	$\lambda_{TPB}^{A}i_{trans}^{an}$	$\lambda_{TPB}^{A}i_{trans}^{ca}$	Insulation

List of Figures

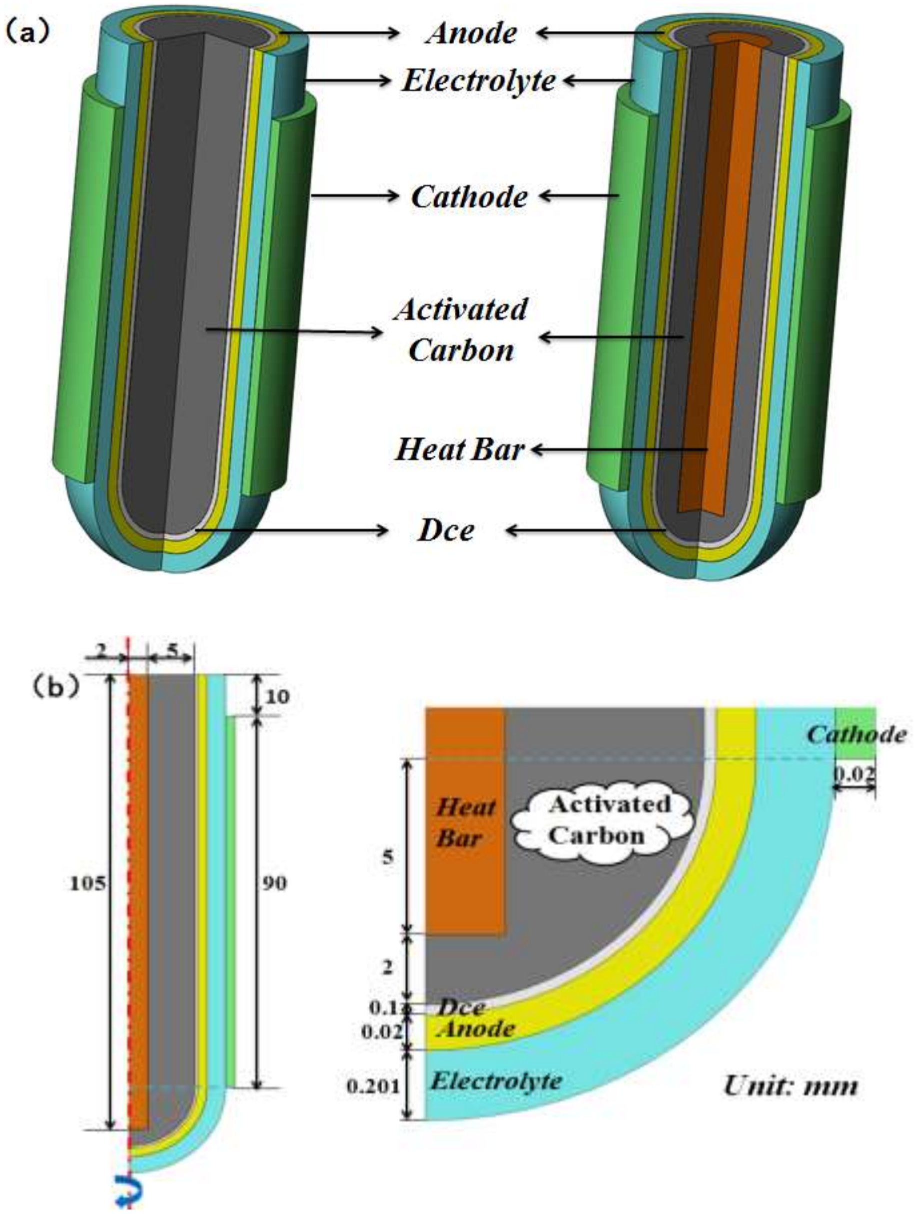

Fig .1 schematic of tubular DC-SOFC (a) without and with heat bar, (b) the simulation domain and detailed size of the model

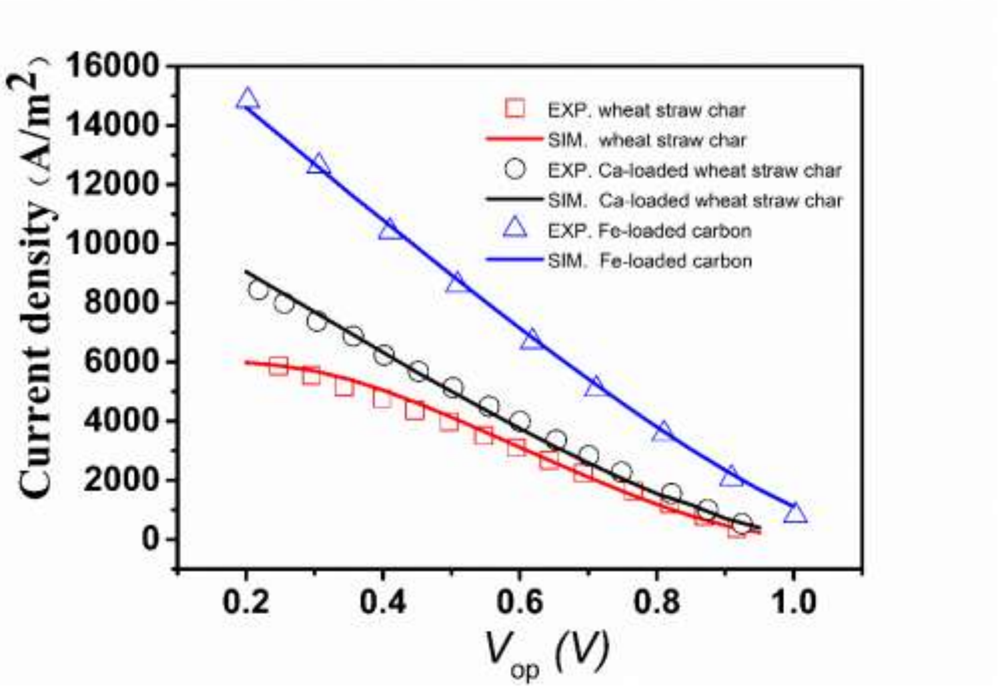

Fig. 2 Validation of model

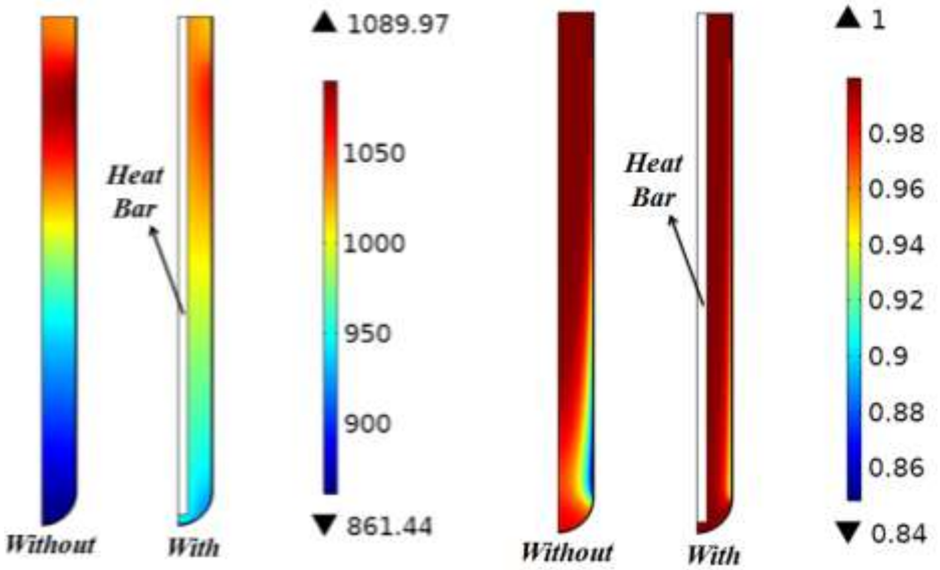

(a) Temperature (b) CO mass fraction

Fig. 3 The distribution of (a) temperature and (b) CO mass fraction of carbon chamber

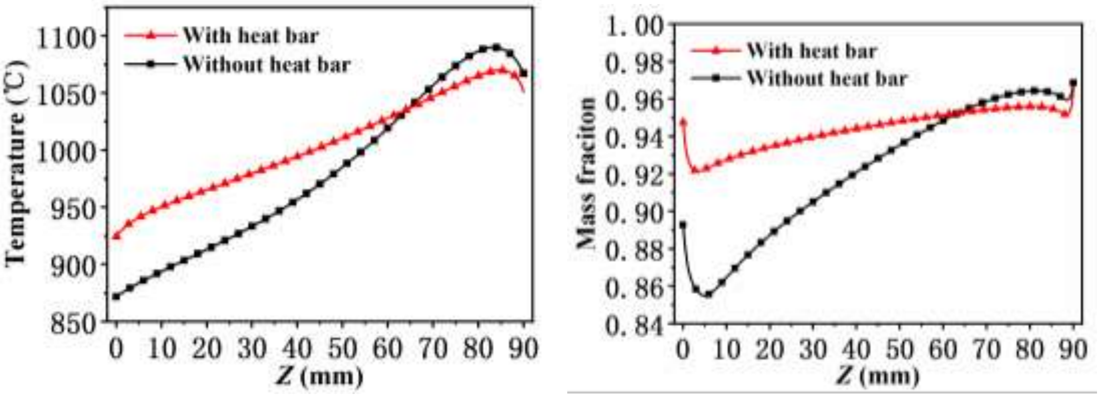

(a) Temperature (b) CO mass fraction

Fig. 4(a) The temperature and (b) The CO mass fraction distribution at the anode surface

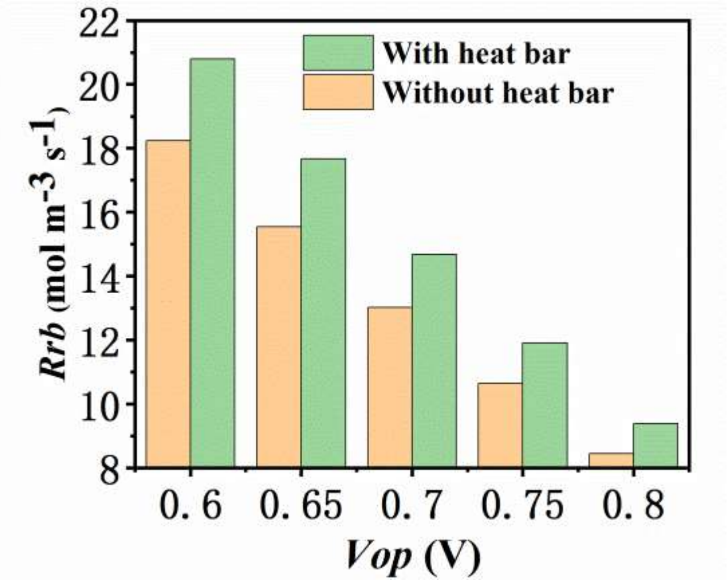

Fig. 5 The average volumetric Boudouard reation rate

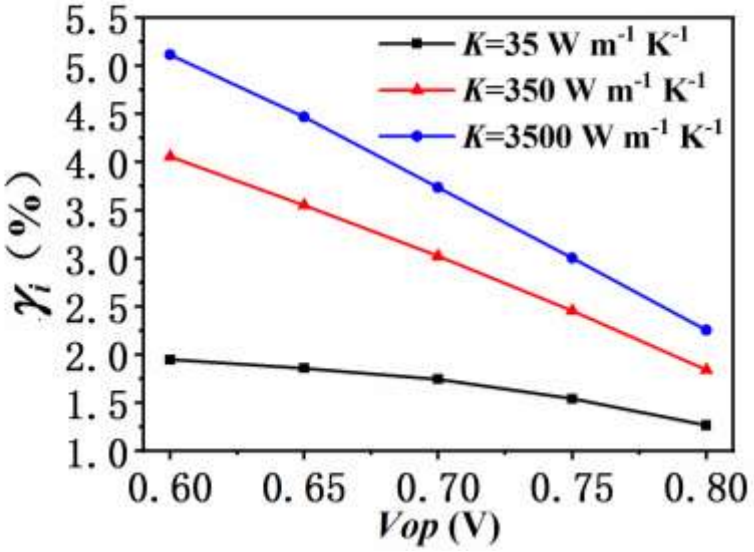

Fig. 6 Dependence of the growth rate γ_i on the heat bar thermal conductivity

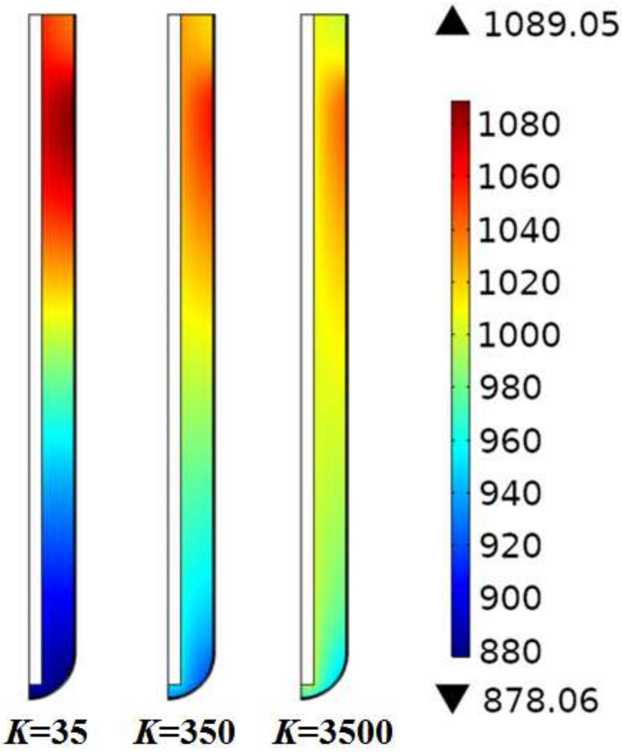

Fig. 7 The temperature distribution in carbon chamber

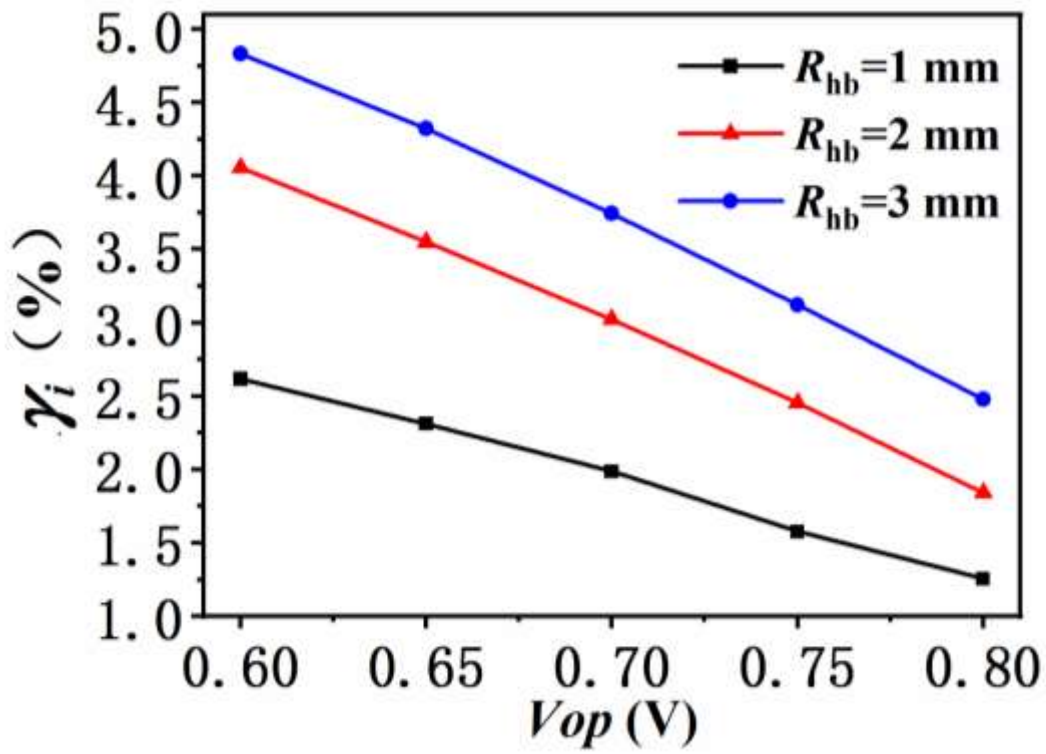

Fig. 8 Dependence of the growth rate γ_i on R_{hb}

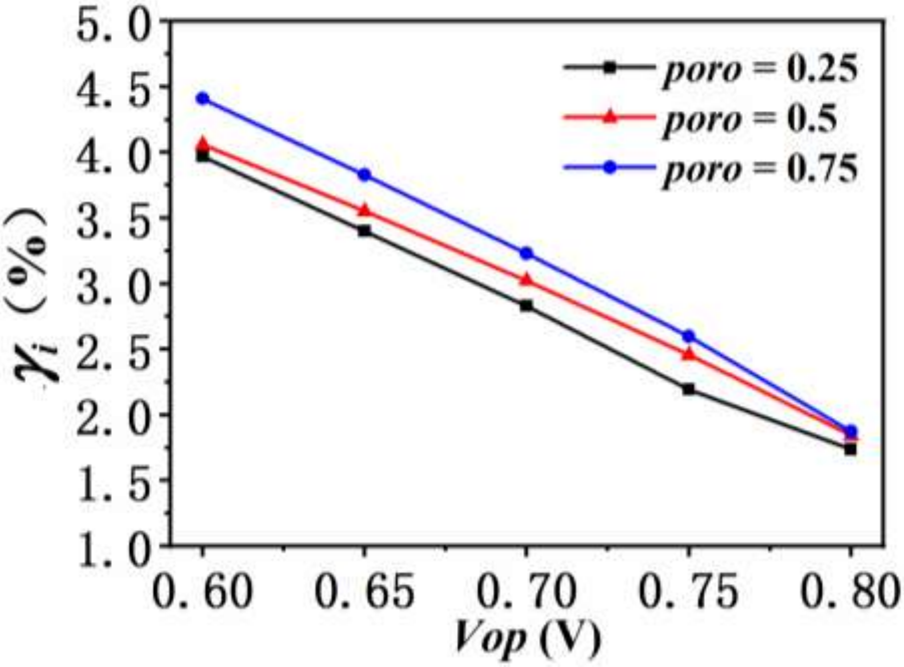

Fig. 9 Dependence of the growth rate γ_i on the carbon chamber porosity